

Self-Assembly of Quantum-Confined CsPbBr₃ Perovskite Nanocrystals into Rhombic, Frame, and Rectangular Superlattices

Matheus Gomes Ferreira, Baptiste Gastin, Jonas Hiller, Ivan A. Zaluzhnyy, Gerard N. Hinsley, Bihan Wang, Kuan Hoon Ngoi, Ivan A. Vartanyants, Frank Schreiber, Marcus Scheele, and Dmitry Baranov*


Superlattices of quantum-confined perovskite nanocrystals (5–6 nm) present an interesting example of colloidal crystals because of the interplay between nanoscopic parameters (nanocrystal sizes, shapes, and colloidal softness) and the microscopic shapes of their assemblies. These superlattices are reported as rectangular or rhombic, with little discussion of the outcomes of self-assembly experiments which are worthwhile to study given the rising interest in the optical properties of these nanomaterials. It is observed that various superlattice shapes are produced in a single solvent evaporation experiment from a nanocrystal dispersion drop-casted onto a tilted substrate. The observed shapes are categorized as rhombi, rectangles, and hollow frames (including hollow rectangular frames, nested structures, and interconnected fragments). The influence of self-assembly conditions is studied by optical microscopy, and the nanocrystal circularity, aspect ratio, and size are quantified by transmission electron microscopy with additional insights into the superlattice structure provided by X-ray nanodiffraction. The results suggest that rhombic shapes arise from a subpopulation of nanocrystals with broader size and shape dispersions, whereas more uniform nanocrystals form rectangular structures (either solid or hollow). The solvent evaporation dynamics and diffusion of the drying liquid contribute to forming more complex shapes, such as nested frames and cracked and multidomain superlattices.

1. Introduction

Self-assembly of quantum-confined lead-halide perovskite nanocrystals into superlattices is a rapidly developing area of research motivated by the pursuit of collective properties. Many studies focus on the self-assembly of weakly confined CsPbBr₃ nanocrystals due to the reported observation of collective properties in luminescence and X-ray diffraction.^[1–6] Theoretical predictions indicate the largest enhancement of collective light emission (e.g., superradiance) in the assemblies of smaller, strongly confined nanocrystals,^[7–9] due to the stronger radiative coupling.^[9] The self-assembly requires uniform nanocrystals, and thanks to the synthetic development of recipes yielding nanocrystals with narrow size distributions,^[10,11] batches with an average size of around 6 nm in a strong quantum confinement regime (below ≈ 7 nm Bohr exciton radius of CsPbBr₃^[12–15]) are available. Consequently, self-assembly into superlattices and investigations of collective light emission such as superradiance followed.^[16,17] Specifically, the quantum-confined CsPbBr₃ nanocrystals

M. Gomes Ferreira, D. Baranov
Division of Chemical Physics and NanoLund
Department of Chemistry
Lund University
P.O. Box 124, Lund SE-221 00, Sweden
E-mail: dmitry.baranov@chemphys.lu.se

B. Gastin
École Supérieure d'Ingénieurs de Rennes
Campus de Beaulieu - Bâtiment B41 - B41 bis - B42 263 avenue du Général
Leclerc, 35042 Rennes Cedex, France

 The ORCID identification number(s) for the author(s) of this article can be found under <https://doi.org/10.1002/ssstr.202500133>.

© 2025 The Author(s). Small Structures published by Wiley-VCH GmbH. This is an open access article under the terms of the Creative Commons Attribution License, which permits use, distribution and reproduction in any medium, provided the original work is properly cited.

DOI: 10.1002/ssstr.202500133

J. Hiller, M. Scheele
Institute for Physical and Theoretical Chemistry
University of Tübingen
Auf der Morgenstelle 18, D-72076 Tübingen, Germany

I. A. Zaluzhnyy, F. Schreiber
Institut for Applied Physics
University of Tübingen
Auf der Morgenstelle 10, D-72076 Tübingen, Germany

G. N. Hinsley, B. Wang, K. H. Ngoi, I. A. Vartanyants
Photon Science
Deutsches Elektronen-Synchrotron DESY
Notkestraße 85, D-22607 Hamburg, Germany

derived from the ZnBr_2 -mediated syntheses have been reported to self-assemble into rectangular^[10,16–18] and less common rhombic superlattices.^[19] These observations of different superlattice morphologies obtained from nanocrystals derived from nominally similar syntheses suggest that there are factors, either intrinsic to the nanocrystals or external to the self-assembly conditions, that influence the superlattice shapes. Ideally, one would like to predict the shape of the superlattice based on the initial conditions and properties of nanocrystal batches, for example, average size, shape, and other characteristics. However, predicting colloidal self-assembly is notoriously difficult due to the many variables influencing self-assembly and small energy differences between competing packing modes of polyhedral particles.^[20] As a result, researchers are often left with trial-and-error experimentation to empirically explore the diversity of superlattices and study their physical properties.

Such experimentation is fruitful, as evidenced by several examples. Rupich et al. observed size-dependent twinning in PbS superlattices by systematic assembly of a series of PbS colloids of different sizes.^[21] In that work, PbS nanocrystals larger than 7 nm produced twinned superlattices, while nanocrystals smaller than 4 nm self-assembled without twinning. Huang et al. monitored stages of antisolvent diffusion-induced colloidal crystallization of octahedrally shaped 10.5 nm PbS nanocrystals.^[22] In that study, superlattices went from rhombic to triangular shapes, including multidomain “butterfly” shapes, as their size increased from a few microns to several tens of microns. The different consecutive growth mechanisms (from classical nucleation and growth to seeded secondary growth and oriented attachment), along with changes in the nanocrystal packing from body-centered cubic (bcc) to face-centered cubic (fcc), have been used to rationalize these observations.^[22] Different polyhedral shapes in the colloidal assembly of noble metal nanocrystals have been known for a while, with examples of single-component and binary nanocrystal superlattices self-assembled into macroscopic polyhedra such as truncated pyramids, hexagons, and octahedra, among others.^[23–25] With lead halide perovskite nanocrystals, most of the works have been dedicated to rectangular superlattices and aggregates grown by solvent evaporation on flat substrates,^[18,26–29] in the liquid phase,^[30–32] by templating,^[33–35] and rounded superlattices formed under spherical confinement.^[36,37] The shape appears to affect function, although the evidence is presently limited due to the novelty of the material. The perovskite nanocrystal superlattices of spherical shapes showed properties different from rectangular ones, such as Mie resonances, which accelerated photoluminescence (PL) and reported polaritonic effects at cryogenic temperatures,^[38] different from the optical properties of rectangular superlattices at low temperatures explained by collective superfluorescence and superradiance.^[16,17,28,39–41] Besides rectangular, rhombic, and spherical shapes, a report of pyramid-shaped superlattices with a rectangular base and superfluorescence is emerging as well.^[42]

Motivated by recent advances and theoretical predictions, we explored the self-assembly of small (5–6 nm) CsPbBr_3 nanocrystals synthesized via a ZnBr_2 -mediated approach. After optimizing the synthesis and isolation processes, we found that solvent evaporation led to the formation of various superlattice shapes from the same nanocrystal batch on a single substrate. This work pursues several key objectives: first, to detail the synthesis and

isolation of nanocrystals suitable for superlattice formation; second, to examine how sample preparation steps such as filtering, dilution, and the addition of extra solvent affect self-assembly outcomes; and third, to investigate the factors driving superlattice shape variation through direct observations, nanocrystal characterization, and X-ray nanodiffraction studies on individual superlattices. Overall, this study aims to deepen the understanding of colloidal perovskite nanocrystal self-assembly under common experimental conditions.

2. Results

2.1. Nanocrystals and Self-Assembly

The as-synthesized and isolated CsPbBr_3 nanocrystals show a pronounced lowest energy exciton peak in the absorption spectrum at 486 nm (2.55 eV) (Figure 1a, dark blue curve), corresponding to an average size of ≈ 5.8 nm, obtained from the sizing curve of Brennan et al. correlating absorption peak with electron microscopy sizes.^[43,44] This edge length puts these nanocrystals into the strongly confined regime. The pronounced and well-defined shape of the lowest energy absorption peaks, assigned to the s-s and p-p excitonic transitions,^[11,45,46] with two discernible peaks at higher energy, indicates a narrow size distribution of the nanocrystal ensemble. The PL spectrum has a maximum of 498 nm (2.490 eV) with a full-width at half maximum of 110 meV (Figure 1a, light blue curve). From the self-assembly perspective, 5.8 nm CsPbBr_3 nanocrystals capped with oleic acid and oleylamine ligands are softer compared to larger, weakly confined nanocrystals with edge lengths in the range of 8–10 nm. The estimated softness of nanocrystals in this work is $S = 2L/a = 3.6 \text{ nm}/5.8 \text{ nm} = 0.62$, where L is the estimated ligand length and a is the nanocrystal size. Overall, nanocrystal samples used for assembly experiments in this work are largely congruent with as-synthesized nanocrystals derived from ZnBr_2 -assisted synthesis in other works.

Upon deposition of 40 μL of the nanocrystal dispersion onto a tilted (2.7°) microscope glass slide of $1.5 \times 2.5 \text{ cm}$ dimensions and complete solvent evaporation in a loosely closed Petri dish (Figure 1b), a surprising variety of superlattice shapes were observed (Figure 1c). At the top of the substrate, the well-isolated superlattices of rhombic shapes (estimated obtuse angle = $105 \pm 3^\circ$) were formed. In the middle of the substrate, the shapes became more polygonal with numerous kinks, and superlattices increased in thickness by showing a stronger contrast with the background. At the bottom of the substrate, where in the tilted configuration the amount of nanocrystal dispersion is the largest, the primarily rectangular superlattices on top of a continuous film have been formed. Tilting the substrate creates a spatially resolved concentration gradient during nanocrystal assembly. At 0° (no tilt), the dispersion dries via the coffee-stain effect, with nanocrystals accumulating at the droplet edges to form a thick film and superlattices on top. At higher angles (5.4° and 8.2°), the assembly is similar to 2.7° , but the concentration gradient is confined to a shorter region along the substrate due to liquid accumulation near the bottom of the substrate. Thus, a moderate tilt angle allows spatially resolved observation of superlattices,

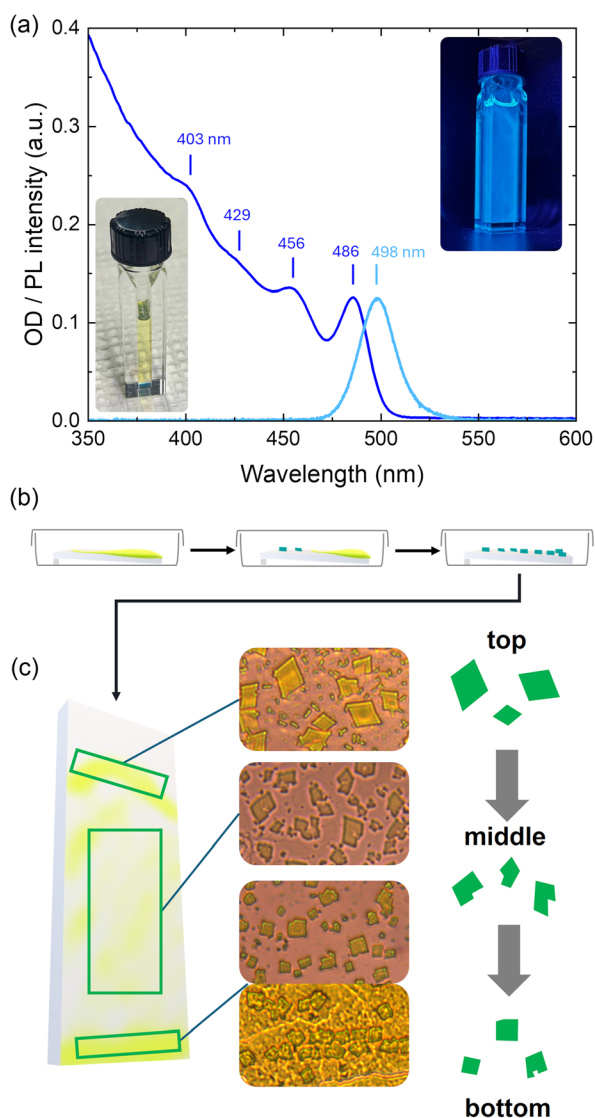


Figure 1. a) Optical absorption (dark blue curve) with four discernible transitions marked at 486 nm (2.55 eV), 456 nm (2.72 eV), 429 nm (2.89 eV), and 403 nm (3.08 eV) and PL spectra (light blue curve, $\lambda_{\text{exc}} = 385$ nm) of CsPbBr₃ nanocrystals in dilute toluene dispersion, the left inset shows a photograph of dilute nanocrystal dispersion under the room light, and the right inset shows a photograph of it under UV flashlight. b) Sketch of the self-assembly setup on a tilted (2.7°) glass slide, illustrating the gradual drying of the sessile drop of the nanocrystal dispersion. c) A variety of superlattice habits were observed along the length of the substrate from top to bottom under an optical microscope (40× objective) in a single experiment. Two images in the bottom part of the sample illustrate isolated superlattices just before the edge of the drying liquid and superlattices together with continuous nanocrystal solid film at the dried edge.

and beyond 2.7°, the region of assembly simply becomes shorter and less convenient to work with.

The portion of nanocrystal superlattices from the top region of the substrate where rhombic-shaped superlattices were observed was dissolved in a small volume of toluene and the absorption spectra of that fraction were compared with the absorption spectra from the starting nanocrystal dispersion. After scaling the

absorption spectra to compensate for differences in nanocrystal concentrations, the spectra were found to overlap with each other (see Supporting Information Figure S6), indicating minimal differences between the nanocrystals in the rhombic superlattices and the starting solution. At the same time, the optical microscopy results clearly show various superlattice shapes formed from the same batch of nanocrystals in a single experiment.

2.2. Diversity of Superlattice Shapes (Habits)

After performing the growth of superlattices made by the same synthesis protocol with minor changes in superlattice growth conditions and inspecting them under an optical microscope, it was observed that a single batch of synthesized nanocrystals with seemingly high size homogeneity could produce a variety of superlattice shapes. To explore what other shapes are possible, we chose to vary several experimental parameters, always using the nanocrystal batches synthesized in the same way. The optimized experiment led us to 12 samples with interconnected variable changes, and the following major superlattice shapes have been observed: rhombi, rectangles, squares, and hollow frames (Figure 2). The superlattices with perfect sides were rare, and the majority of superlattices showed kinks, cracks, a combination of rounded and sharp corners, and rectangular inclusions inside the hollow frames (i.e., a smaller rectangular superlattice within a larger hollow frame superlattice). We note that across 44 experiments (32 preliminary plus 12 optimized), among the isolated superlattices with discernible geometrical shapes, rhombi have been observed with an approximate frequency of 31%, rectangles and squares at 47%, and frames at 22%. Besides these shapes, all the samples featured variable amounts of aggregates of superlattices, superlattices merged in irregular formations, and the dried residue of continuous nanocrystal films.

Table S1 in the Supporting Information lists the samples and varied conditions, and their optical microscopy images are shown in Supporting Information Figure S7–S10, including the division into three regions of interest along the substrate (top, middle, and bottom). The self-assembly on a tilted substrate and the resulting spatial resolution in the concentration of the drying nanocrystal dispersion provide additional context for the interpretation of the results. Figure 2 presents an overview of the collected data from the prepared samples, in which the superlattices of three principal morphologies are illustrated. Both rhombic and rectangular shapes have been previously reported,^[17,19] while hollow frames from perovskite nanocrystals have been observed, but not reported before.

2.2.1. Rhombi

Analyzing the formation of rhombic superlattices under various growth conditions revealed several key influences. Both filtered and nonfiltered nanocrystal dispersions exhibited similar absorption spectra; however, the concentration in the filtered sample was lower by about 4 μM ($\approx 30\%$) due to the removal of large aggregates by the polytetrafluoroethylene (PTFE) filter. Optical images (see Supporting Information Figure S7–S10) show that nanocrystal concentration and the addition of extra toluene in

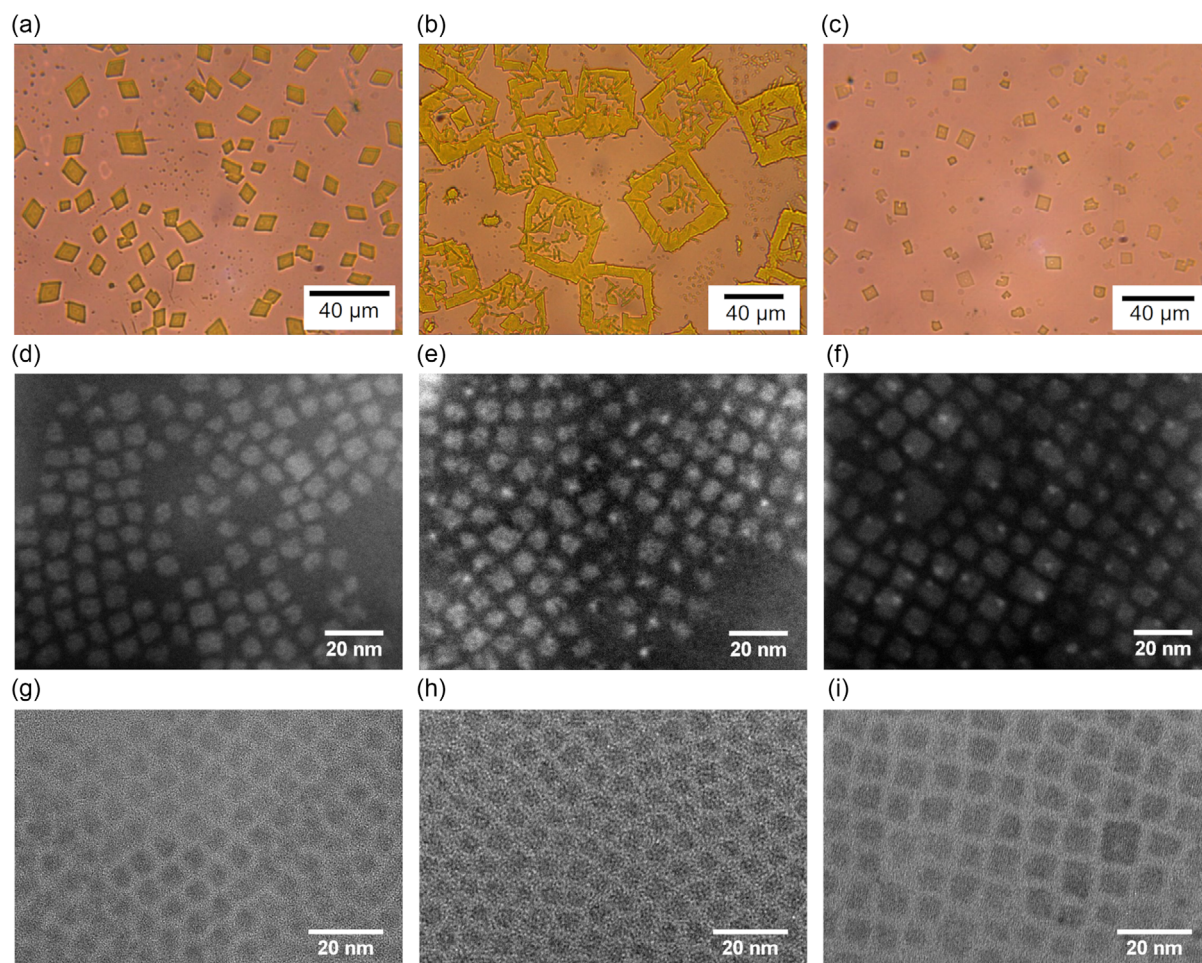


Figure 2. The microscopy overview of CsPbBr_3 nanocrystal superlattices of different habits. a–c) Optical micrographs of the rhombic, frame, and rectangular superlattices; d–f) STEM images of the dissolved superlattices of rhombic, frame, and rectangular habits, respectively; g–i) bright-field TEM of the dissolved superlattices of the rhombic, frame, and rectangular habits, respectively.

the Petri dish, which affects toluene vapor saturation and the evaporation rate of the sample, influence the rhombic superlattice formation. Samples containing extra toluene produced more rhombic superlattices across all dilutions (1:1, 3:1, 5:1), and these superlattices appeared in the middle region of the substrate only when extra toluene was present. Furthermore, samples with higher initial nanocrystal concentrations (nonfiltered) yielded more rhombic superlattices compared to those grown from filtered dispersions.

In the top and bottom regions of the substrate, larger rhombic superlattices formed due to higher nanocrystal concentrations during drying, as this is influenced by the pinning of the evaporation front, diffusion, convection, capillary action, and gravity.^[47] The top region has a thinner liquid layer because of tilting, leading to faster evaporation but higher nanocrystal concentration from capillary forces pulling the nanocrystals upward. The bottom region contains a thicker layer of liquid with more material and potential precipitation of nanocrystal aggregates by gravity. Optical images indicate that extra toluene causes larger superlattices and more cracks, possibly due to drying-induced contraction or dissolution-recrystallization. As observed visually

and in Video S1–S3, Supporting Information, for a sample drying in air, the evaporating liquid front recedes unevenly through cyclical crystallization-dissolution. We hypothesize that this process contributes to superlattice fragmentation, crack formation, and the emergence of domains that eventually merge into bigger, less regular structures in a closed Petri dish (see Supporting Information Figure S11).

2.2.2. Frames

Figure 2b and **3** highlight surprising and unexpected superlattice shapes referred to as “frames.” These were observed primarily in samples prepared with filtered nanocrystal dispersions at the 3:1 dilution and extra toluene in the Petri dish. Frames with sharp edges appear in all three regions of the substrate, sometimes as isolated frames and sometimes interconnected (Figure 3a–c). Curiously, small rectangular superlattices or rod-like crystals could sometimes be found at the center of frames (Figure 3d–f). Filtered samples without extra toluene showed no frame-shaped superlattices under any concentration; when nonfiltered dispersions were used with extra toluene, no frame-shaped

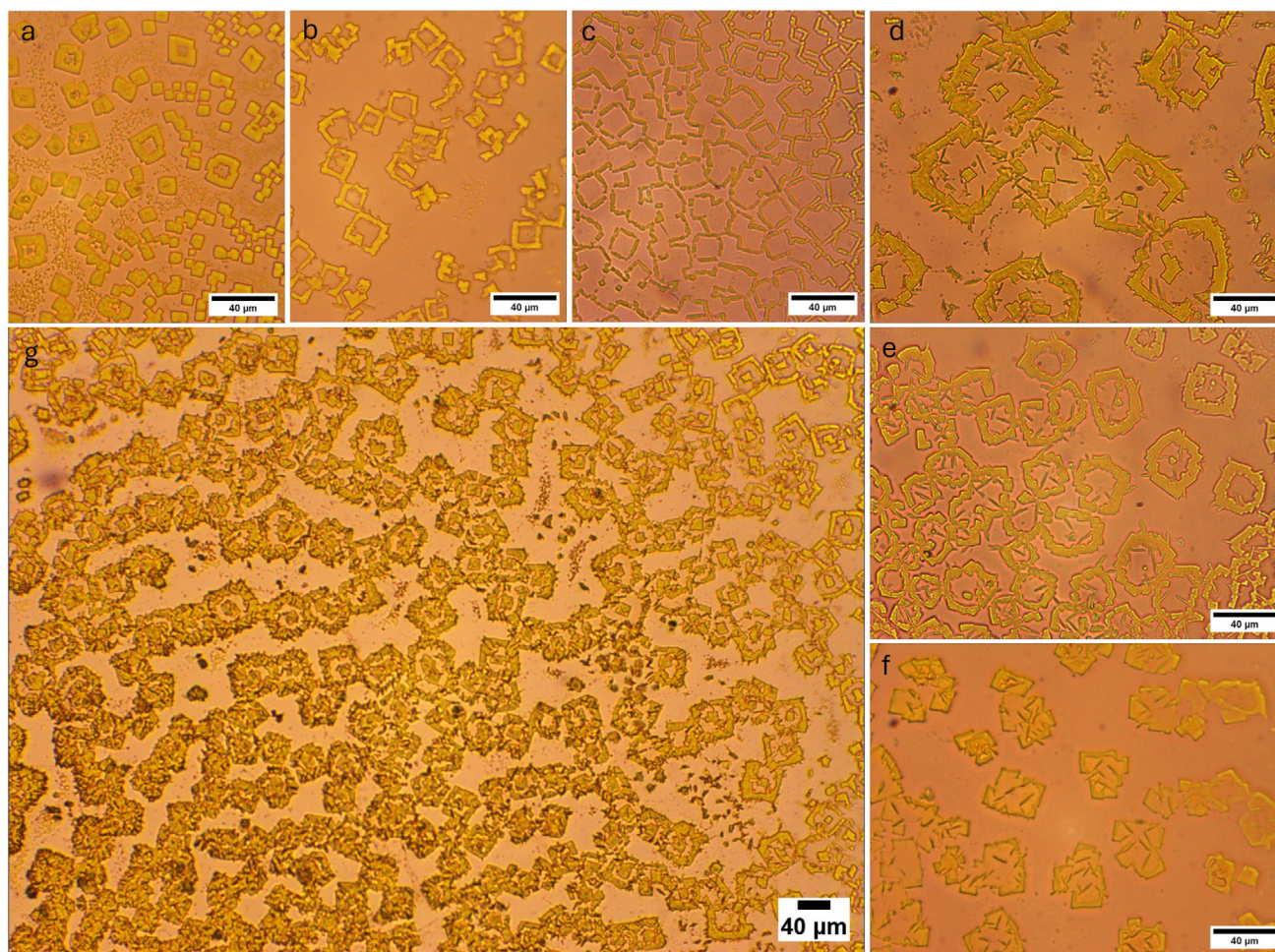


Figure 3. Variety of frame superlattices observed by optical microscopy: a–c) isolated and interconnected frames with thick and thin boundaries, d–f) nested superlattices with square and rod-like inclusions and their combinations, and g) an overview of the large sample area covered with numerous nested frame superlattices. The images are displayed with an increased contrast, all scale bars are 40 μm .

superlattices were found as well. However, nonfiltered concentrated samples (dilution 1:1) without extra toluene yielded frames ranging from large rectangular-/rhombic-shaped frames in the top region to smaller rectangular frames in the middle and bottom of the substrate. Interestingly, a few larger frames in the top region showed a spiral-like progression toward the center of the structure (see Supporting Information Figure S11).

The apparent correlation of frames with filtration and extra toluene during the sample evaporation made us hypothesize that slow drying with excess solvent, removal of aggregates, and spurious macroscopic impurities are key factors behind the frame formation. The spiral-like structures suggest the drying of nanocrystal dispersion did not proceed radially inward. The drying liquid front was probably interrupted by superlattice formation, trapping portions of the liquid inside and creating rectangular basins, where nested superlattices formed as a result of diffusion and evaporation.^[48] In related observations, the round hollow assemblies of colloidal nanorods dried from water dispersions on a superhydrophobic surface at high humidity were reported by Accardo et al.^[49] and rationalized by convective flows pushing

the solid residue toward the pinned line at the edge of the droplet, with the central area remaining empty due to the low wettability and adherence of the material to the substrate. Similar effects could be at play in the case of perovskite nanocrystal superlattice frames, as the drying in solvent vapor atmosphere may proceed through the formation of localized microdroplets, and similar material redistribution, as the empty areas around superlattices in all of the observations suggest that nanocrystals do not wet the surface of the glass but tend to roll off it. Another comparison could be made with the formation of hopper-shaped inorganic crystals such as NaCl. In that case, the hollow crystals form because supersaturation and material deposition happen faster at the edges or corners of the growing crystal than at its center.^[50,51] The exact analogy seems not applicable here as the frame superlattices look fragmented, unlike single crystals of NaCl. These observations point to complex local self-assembly dynamics at the length scales of tens of microns that contribute to the formation of the frames, which are affected by the solvent vapors and the supersaturation of drying nanocrystal dispersion.

2.2.3. Rectangles

Figure 2c shows superlattices exhibiting predominantly rectangular habits. From optical image analysis, changes in the experimental parameters did not substantially affect the rectangular shape of the superlattices. The main difference was in their size: extra toluene in the Petri dish yielded larger rectangular superlattices across all regions. However, many of these rectangular superlattices feature slight angular distortions or rounded edges. Initial inspection of EM images (Figure 2d–i) of nanocrystals from selectively dissolved superlattices of different shapes indicates that the nanocrystals from rectangular superlattices show square and rectangular outlines, while other nanocrystal populations feature more irregular shapes and packing. Further analysis and possible connections between nanocrystal shapes and superlattice habits are discussed in the next sections.

2.2.4. Influence of Extra Solvent

To study the influence of an extra solvent in the Petri dish, a 3:1 dilution of the nanocrystal stock solution with toluene was chosen, and the atmosphere was saturated with either toluene, hexane, ethyl acetate, or tetrachloroethylene (see Supporting Information Figure S12). Overall, the superlattices were predominantly rhombic or rectangular, but each solvent yielded differences. In hexane, the superlattices were generally smaller, uniform, and distributed evenly across the top, middle, and bottom of the substrate, with the bottom region showing a larger amount of material due to the effects already discussed above. In toluene, larger and more distinctly rhombic superlattices formed, exhibiting noticeable cracks. In tetrachloroethylene, the superlattices appeared thicker and bulkier, with holes instead of cracks in one region. The formation of holes could be due to the condensation of heavier tetrachloroethylene droplets onto the superlattices during drying (tetrachloroethylene density 1.62 versus 0.866 g cm⁻³ for toluene). In ethyl acetate, the superlattices appeared larger than those formed with hexane, possibly due to the antisolvent properties of ethyl acetate.

2.3. Nanocrystal Dimensions from Electron Microscopy

The selective dissolution of superlattices with different habits was followed by electron microscopy imaging of the resulting nanocrystals. This allowed for a comparison of their 2D projections to identify any potential significant differences. Visual inspection and comparison of fast fourier transform (FFT) of the scanning transmission electron microscopy (STEM) images indicated that nanocrystals from rhombic superlattices exhibit a mixture of rectangular and irregular nanocrystal projections with hexagonal or significantly distorted square packing (Figure 2d, see Supporting Information Figure S13). Nanocrystals from rectangular and frame superlattices predominantly display rectangular close-to-square projections with square or distorted square packing with the nearest neighbor (Figure 2e,f, see Supporting Information, Figure S14, S15). These differences align with the macroscopic shapes: rhombic superlattices lacked right angles characteristic of square packing, while frame superlattices, though hollow, were generally rectangular or square (Figure 3)

and more like rectangular ones. To further quantify the observations, images were processed using ImageJ.^[52] The STEM images were chosen due to their higher contrast compared to bright-field transmission electron microscopy (TEM) images and the nanocrystal outlines were extracted by applying a smoothing filter (FFT bandpass filter) and thresholding, followed by the automated quantification of the resulting outlines. Details of the procedure are provided in the Supporting Information (see Supporting Information Figure S16) and prior works,^[53,54] the STEM images and the associated data are available in the dataset accompanying this work.^[55]

Among the various parameters measured by ImageJ, circularity, aspect ratio (AR), and the area of nanocrystals have been compared between the nanocrystal populations for significant differences. Circularity is defined as $C = 4\pi \cdot A_{NC}/p_{NC}^2$, where A_{NC} is the area of the nanocrystal outline and p_{NC} is its perimeter, while the AR is the ratio of the major to minor radii of the ellipse fitted to the nanocrystal outline. For reference, $C = 1$ for an ideal circle and $C = 0.785$ for an ideal square, with lower values indicating more elongated particles. In all three populations, circularity was concentrated in the 0.8–0.9 range, which is higher than one would expect for squares or anisotropic rectangles. The value of the extracted circularity depends on the pixel resolution, image signal-to-noise ratio, and the degree of smoothing introduced by the FFT bandpass filter and thresholding steps. There is a trade-off here: minimal filtering leads to grainier outlines with larger perimeters (and thus artificially lower C), whereas stronger filtering rounds the outlines and inflates C . Based on the FFT comparison discussed above, we selected filter parameters that yielded an average circularity close to that of an ideal square for nanocrystals from rectangular superlattices. The obtained mean parameter values ($\mu_{A_{NC}}$, μ_C , μ_{AR}) for the extracted nanocrystal parameters are as follows: rhombic superlattices ($\mu_{A_{NC}} = 35 \pm 10 \text{ nm}^2$, $\mu_C = 0.76 \pm 0.11$, $\mu_{AR} = 1.30 \pm 0.29$), rectangular superlattices ($\mu_{A_{NC}} = 35 \pm 11 \text{ nm}^2$, $\mu_C = 0.78 \pm 0.08$, $\mu_{AR} = 1.31 \pm 0.23$), and frame ($\mu_{A_{NC}} = 27 \pm 7 \text{ nm}^2$, $\mu_C = 0.76 \pm 0.09$, $\mu_{AR} = 1.33 \pm 0.22$). The value of mean area agrees well with a square of the nanocrystal size estimated from the absorption spectrum, $a^2 = (5.8 \text{ nm})^2 \approx 34 \text{ nm}^2$ (see Section 2.1), confirming that sizing curve is a reliable tool for estimating the average nanocrystal size. **Figure 4** illustrates the distribution of parameters as a 3D density plot (2D correlation plots are shown in Supporting Information Figure S17–S19). Comparing the mean values, the biggest differences are smaller areas of nanocrystals from frame superlattices and slightly wider spreads of the AR and circularity values for the nanocrystals from rhombic superlattices as compared to the rectangular and frame ones. The comparison of the relative volumes (V_{rel}) of the 3D ellipsoids fitted to the parameter distribution plots reveals that the volume of the parameter ellipsoid for nanocrystals from rhombic superlattices is ≈ 1.6 times bigger than for rectangular and 2.15 times bigger than for the frame superlattices. This is an indication of a larger variety of nanocrystal projections for nanocrystals from rhombic superlattices as compared to their rectangular and square counterparts. We attribute such variation of nanocrystal projections to the variation of underlying 3D nanocrystal shapes, possibly indicating that the population of nanocrystals that self-assemble into rhombic superlattices deviate from rectangular cuboidal or oblate parallelepiped shapes^[19] toward more

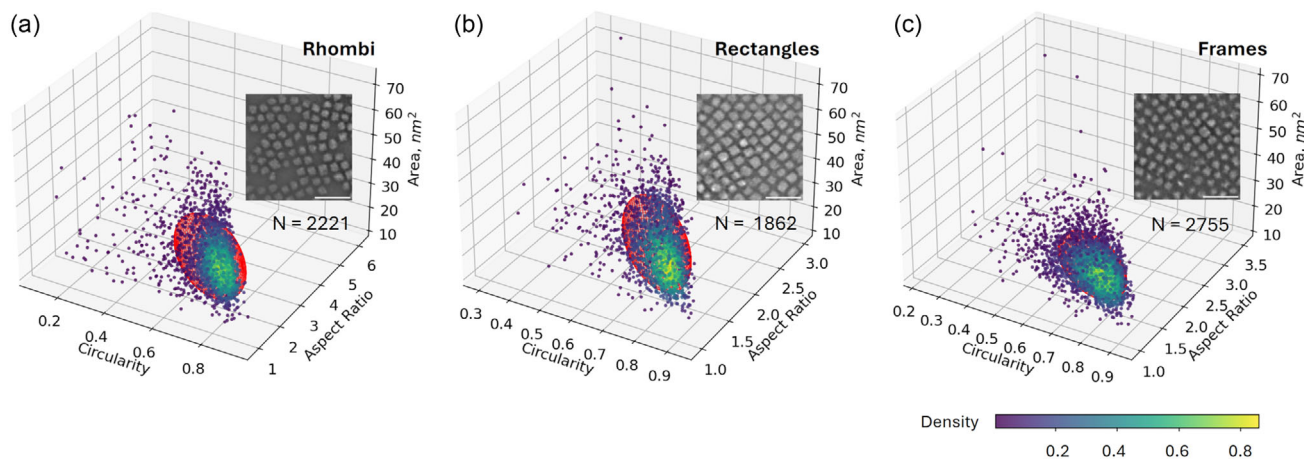


Figure 4. 3D correlation plots of circularity, aspect ratio, and area of nanocrystals from dissolved superlattices of different habits with fitted ellipsoids (red contours) with center coordinates at mean parameter values μ_{AR} , μ_{C} , and μ_{AR} : a) rhombi (ellipsoid radii, $r_1 = 15.6$, $r_2 = 0.45$, $r_3 = 0.13$, $V_{\text{rel}} = 2.15$ a.u.), b) rectangles ($r_1 = 16.6$, $r_2 = 0.35$, $r_3 = 0.10$, $V_{\text{rel}} = 1.37$ a.u.), and c) frames (ellipsoid radii, $r_1 = 10.4$, $r_2 = 0.34$, $r_3 = 0.12$, $V_{\text{rel}} = 1$ a.u.). Insets show FFT-filtered areas of STEM images for respective samples. The scale bar is 30 nm.

truncated geometries. We recognize that inferring 3D shapes from 2D projections must be done with caution and will require additional confirmation.^[56] To gain deeper insight, a different approach shall be considered. For example, one possibility is to combine in situ observations of nanocrystal assembly by electron microscopy^[57,58] with 3D atomic structure reconstruction in liquid.^[59,60] The STEM results discussed here serve as an indication of the origins of different superlattice habits and motivation to seek sophisticated techniques in the future.

2.4. Insight into the Superlattice Structure by X-Ray Nanodiffraction

To gain further insight into the correlation between superlattice habit and structure, isolated superlattices were studied with X-ray nanodiffraction. Complete data acquisition and analysis details are provided in the Supporting Information and Supporting Information Figure S21–23. **Figure 5** shows the results of small-angle X-ray scattering (SAXS) experiments performed on

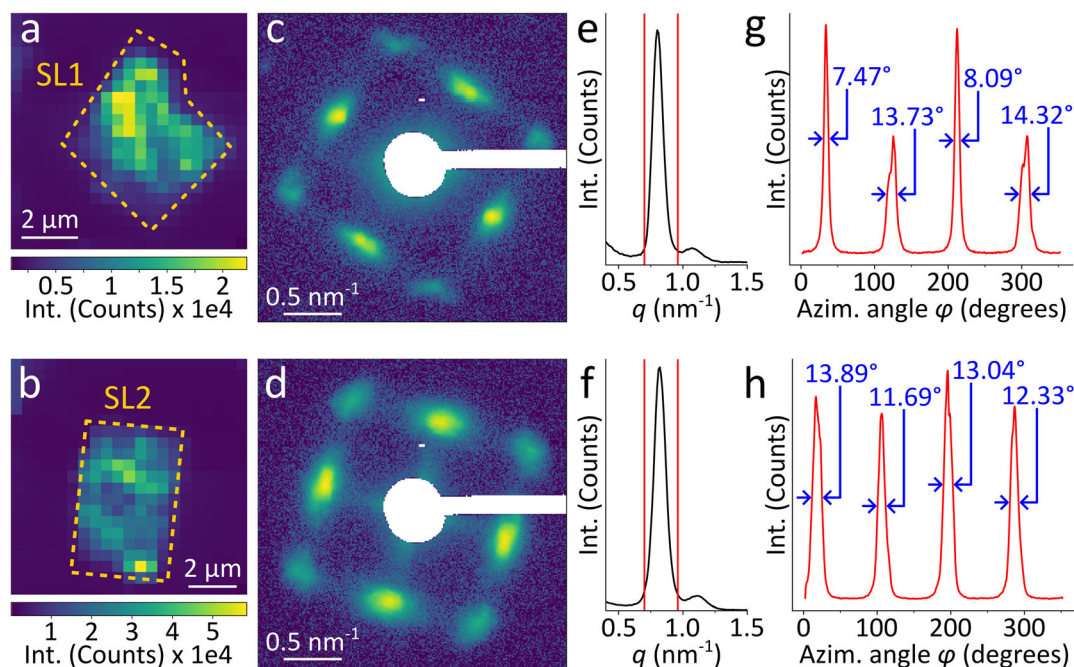


Figure 5. Spatially resolved SAXS recorded from two isolated superlattices with morphologies close to rhombic (SL1, top) and rectangular (SL2, bottom). a,b) SAXS intensity maps of the samples, c,d) spatially averaged SAXS patterns, e,f) corresponding radial profiles with red lines indicating the first order SAXS peaks at $q = 0.70\text{--}0.96\text{ nm}^{-1}$, and g,h) azimuthal profiles of the spatially averaged SAXS intensity averaged over the range $q = 0.70\text{--}0.96\text{ nm}^{-1}$.

two isolated superlattices with habits approximated by a rhombic shape with a kink (SL1, Figure 5a) and a rectangular one (SL2, Figure 5b). The SAXS peak positions are 0.80 nm^{-1} for SL1 and 0.82 nm^{-1} for SL2 for which we obtain lattice constants (inter-nanocrystal periodicity) of 7.85 nm and 7.66 nm , respectively. The small deviation between these two values is expected for superlattices, as they lack a rigid structure and consist of nanocrystals of slightly different sizes interconnected by soft ligands, which can result in slightly different lattice parameters for different superlattices. For both measured superlattices, the lattice constants are $\approx 20\%$ smaller than a nominal sum of the average nanocrystal size from the absorption spectrum and two ligand lengths, $a + 2L = 5.8\text{ nm} + 3.6\text{ nm} = 9.4\text{ nm}$. The difference has been noted previously, such as in the recent comparison of sizing curves, where SAXS systematically underestimated nanocrystal size for CsPbBr_3 nanocrystals in comparison with TEM.^[44] The combination of factors may explain this difference, such as differences in how each measurement technique quantifies dimensions of nanocrystals, the sampled volume, nanocrystal anisotropy, and size segregation specific to self-assembly.^[61,62] The comparison of the azimuthal broadening of the spatially averaged first-order SAXS intensity (Figure 5c–h) revealed that SL1 (rhombic habit) showed a pair of narrower (7.45° and 8.1° , Figure 5g) and broader peaks (13.7° and 14.3° , Figure 5g), while SL2 (rectangular habit) showed four similarly broad peaks ($12.7 \pm 0.9^\circ$, Figure 5h). Building upon the results from the comparative STEM image analysis, we argue that the difference in azimuthal broadening of the SAXS peaks is consistent with a scenario where SL1 has been formed by nanocrystals that are more truncated and elongated as compared to more uniform nanocrystals in SL2. In analogy with colloidal cubes with sharp and rounded corners,^[63–65] rounded nanocrystals would form a slightly oblique lattice, but size dispersion and orientational disorder distort the structure and broaden all four diffraction peaks, as seen in SL2. In contrast, more faceted and anisotropically shaped nanocrystals would form a lattice with smaller orientational disorder, because the misorientation of a single nanocrystal would strongly affect its neighbors, resulting in narrower peaks in SL1. The twinning of the oblique lattice could be responsible for some peaks to double or broaden, as observed for SL1 (see Supporting Information Figure S24).

3. Conclusions

The reported observations lead to several conclusions. One concerns the origin of the different superlattice shapes. Boehme et al.^[19] rationalized the rhombic superlattices of $\approx 5\text{ nm}$ CsPbBr_3 nanocrystals by the colloidal softness of nanocrystals, which accommodates structural distortion and produces obtuse rhombic angles. The variety of superlattice habits observed from a single batch of nanocrystals in our experiments and accompanying differences in nanocrystal dimensions suggest a possibility that the colloidal softness alone may not account for the full diversity of observations and that the nanocrystal shape (such as its deviations from the ideal cubic one by elongation, truncation, or their combination) and its dispersion in a given subpopulation of nanocrystals is another factor. The superlattice habit, that is, its macroscopic shape (rhombic, rectangular, or frame),

results from nanocrystal packing and the consequence of drying dynamics. Theoretical studies of the packing of hard cubes with various degrees of truncation provide additional perspective. Monte Carlo simulations and free-energy calculations of hard cube-shaped particles, progressively truncated toward spheres, show a rich phase diagram, with small differences in truncation capable of changing packing from square to hexagonal,^[66–68] which for nanocrystals could manifest in microscopic superlattice shapes being rectangular or rhombic. A recent simulation considers the transition between a crystalline phase with only translational order (rotator phase) to a phase with translational and rotational order (for example, fully ordered phase) in truncated cubes with small differences in truncation.^[69] In that work, truncated cubes with $s = 0.527$ and 0.572 ($s = 0$ for an ideal cube, $s = 0.5$ for an ideal cuboctahedron, and $s = 1$ for an ideal octahedron) showed different crystal structures: the less truncated cube packed into the hexagonal structure while the more truncated cubes packed into a square structure.^[69] The dispersity of nanocrystal shapes in the experimental samples of small CsPbBr_3 nanocrystals is evident from STEM images and their analysis. The dispersion of nanocrystal shapes may originate from the synthesis and subsequent shape-selective segregation during slow self-assembly on an elongated substrate. Alternatively, because self-assembly is slow (typically the drying was completed overnight) and there is a concentration gradient on the tilted substrate, the nanocrystals could undergo slow reshaping during drying (e.g., nonuniform ligand concentration during solvent evaporation may facilitate surface reconstruction) due to the dynamic surface chemistry.

Concerning the frame-shaped superlattices, explaining their shape by nanocrystal shapes is more challenging. The nanocrystal shape and colloidal softness affect packing locally at the nanoscale, while the frame shapes at the lengthscales of several microns appear to be caused by the macroscopic effect of the material distribution during self-assembly caused by the evaporation dynamics and diffusion. In nanocrystals, frame and hollow shapes originate from chemical reactions (e.g., galvanic replacement,^[70] the Kirkendall effect,^[71] or halide/chalcogen-mediated etching^[72–74]). However, treating superlattice as a single entity that can undergo such a concerted transformation despite its size of several microns or tens of microns lacks experimental evidence. On the other hand, frame-shaped mesostructures or hollow crystals can also be produced by oriented attachment^[75] or hopping, the latter driven by interfacial instabilities that cause edges to grow faster than the center, and reported for colloidal systems.^[76] Presently, the latter seems to be a better explanation. Elucidation of the factors responsible for frame formation is a worthy subject for future work, with the goal of controlling the dimensions and reproducibility of the frame superlattices.

To summarize, in this work, the self-assembly of quantum-confined CsPbBr_3 nanocrystals by slow solvent evaporation revealed that several superlattice habits, such as rhombic, rectangular, and hollow frames, can be obtained from a single nanocrystal batch. Such diversity of superlattice shapes has been attributed to a combination of factors such as deviations from an ideal cubic nanocrystal shape, dispersion of sizes and aspect ratios, a concentration gradient on the tilted substrate, and the presence of excess solvent during self-assembly. Motivated by

the goal of engineering colloidal nanomaterials for collective effects, the results put several aspects of perovskite nanocrystal self-assembly into focus for future work: the correlation between nanocrystal shape and superlattice habit, the origins of unusual superlattice shapes like frames, and possibilities for the shape control of colloidal assembly beyond the ones already observed in the experiments.

4. Experimental Section

The details and the visual guide to the synthesis and assembly of the 5–6 nm CsPbBr₃ nanocrystals, as well as characterization procedures, are described in the Supporting Information (see Supporting Information and Supporting Information Figure S1–S5). Briefly, the nanocrystals were synthesized by adapting the ZnBr₂-assisted method for size control of Dong et al.^[10] The nanocrystal assembly was performed by slow solvent evaporation on a tilted (2.7°) glass substrate from toluene dispersions in a closed Petri dish under ambient conditions. The superlattices were imaged by optical microscopy by using a white-light optical microscope (SAGA) equipped with a digital camera (SJ-U500). The magnification calibration of the optical microscope was done using a Micro-Tec MS33 glass calibration slide (Micro to Nano BV).

Three experimental parameters were interchanged to investigate the influence of each parameter on the final superlattice morphology. The parameters were as follows: 1) nanocrystal concentration [≈ 16 and $11 \mu\text{M}$ of the stock dispersion (unfiltered and filtered through $0.2 \mu\text{m}$ PTFE syringe filter, respectively)], diluted with toluene in 1:1, 3:1, and 5:1 ratios by volume; 2) sample filtration prior to self-assembly; and 3) solvent vapor saturation during the self-assembly by flooding the Petri dish with $350 \mu\text{L}$ of the solvent. For the selective superlattice dissolution, the glass substrates were examined in an optical microscope. Once the area of interest was identified (for example, an area on the glass substrate with predominantly rhombic or other-shaped superlattices), the sample around that area was removed by wiping with a toluene-wetted cotton tip. Then, the superlattices of interest in the remaining area were dispersed in a $15 \mu\text{L}$ drop of toluene using repetitive suction-release action with a micropipette and immediately deposited on a TEM grid for microscopy study.

Absorbance and PL spectra of diluted CsPbBr₃ nanocrystal dispersion in toluene ($10 \mu\text{L}$ of the stock dispersion in $1000 \mu\text{L}$ of toluene) were recorded using a Perkin Elmer Lambda 1050 spectrometer and a fiber-based USB spectrometer (CCS200/M, Thorlabs), equipped with a 420 nm long pass filter (FGL435, Thorlabs) and a 385 nm LED (M385L3, Thorlabs) as excitation source, respectively, using a UV-Quartz $10 \times 4 \text{ mm}$ cuvette, with 4 mm path length. The absorption spectrum was used to determine the average nanocrystal size and nanocrystal concentration using published sizing curves and size-dependent extinction coefficient.^[43,44,77]

TEM in bright-field and STEM modes was performed to characterize the CsPbBr₃ nanocrystals before and after superlattice growth by drop drying $10 \mu\text{L}$ of the concentrated dispersion and $15 \mu\text{L}$ of the dispersion of the redissolved nanocrystals after superlattices growth on an EMR Lacey Carbon support film on copper 300 square mesh grid using a JEOL 300 kV HR-TEM 3000F transmission electron microscope. The STEM images were collected at a magnification of $\times 500\,000$, as they are better suited for nanocrystal shape analysis than bright-field TEM images due to higher contrast.^[53] Attempts to image nanocrystals at higher magnifications led to excessive deposition of carbon in the field of view.

X-ray nanodiffraction experiments on single nanocrystal superlattices were performed on samples grown on flat Kapton substrates by slow solvent evaporation. The samples were scanned with a 13 keV X-ray beam focused to $\approx 300 \times 300 \text{ nm}^2$ spot in transmission geometry using the GINIX endstation^[78] at the Coherence Applications beamline P10 of the PETRA III synchrotron source at DESY.^[79,80] The resulting SAXS diffraction patterns were visualized and processed using a custom-written analysis routine. The complete details are provided in the Supporting Information.

Supporting Information

Supporting Information is available from the Wiley Online Library or from the author.

Acknowledgements

The authors thank Dr. Daniel Madsen and the nCHREM facility at Lund University for assistance with electron microscopy experiments. The authors thank Dr. Stefano Toso for the helpful discussions. The authors acknowledge DESY (Hamburg, Germany) for the provision of experimental facilities. Parts of this research were carried out at PETRA III synchrotron facility. The authors thank Wojciech Roseker and Michael Sprung for their assistance in using the Coherence Application P10 beamline and Tim Salditt for GINIX and the possibility to use it. The work of M.G.F. and D.B. was funded by the European Union (ERC Starting Grant PROMETHEUS, project no. 101039683). Views and opinions expressed are however those of the authors only and do not necessarily reflect those of the European Union or the European Research Council Executive Agency. Neither the European Union nor the granting authority can be held responsible for them. D.B. acknowledges the start-up support from the Faculty of Science, Lund University, and the Crafoord Foundation (decision 20230942). D.B. acknowledges partial support from the grant NSF PHY-2309135 to the Kavli Institute for Theoretical Physics for participation in the KITP Program on Nanoparticle Assemblies: A New Form of Matter with Classical Structure and Quantum Function. M.S., I.Z., and F.S. acknowledge support by the Deutsche Forschungsgemeinschaft (DFG) under grant SCHE1905/9-1 (project no. 426008387), SCHE1905/15-1 (project no. 546072194), and SCHR700/47-1 (project no. 546072194).

Conflict of Interest

The authors declare no conflict of interest.

Author Contributions

Matheus Gomes Ferreira: conceptualization (equal); data curation (lead); formal analysis (equal); investigation (lead); methodology (equal); validation (equal); visualization (equal); writing—original draft (supporting); writing—review and editing (supporting). **Baptiste Gastin:** data curation (supporting); formal analysis (supporting); investigation (supporting); methodology (supporting). **Jonas Hiller:** data curation (equal); formal analysis (equal); investigation (equal); methodology (equal); software (equal); visualization (lead); writing—original draft (supporting); writing—review and editing (supporting). **Ivan A. Zaluzhnyy:** data curation (equal); formal analysis (equal); investigation (equal); methodology (equal); software (equal); visualization (supporting); writing—original draft (supporting); writing—review and editing (supporting). **Gerard N. Hinsley:** methodology (supporting). **Bihan Wang:** methodology (supporting). **Kuan Hoon Ngoi:** methodology (supporting). **Ivan A. Vartanyants:** funding acquisition (supporting); supervision (supporting); writing—review and editing (supporting). **Frank Schreiber:** funding acquisition (supporting); supervision (supporting); writing—review and editing (supporting). **Marcus Scheele:** funding acquisition (supporting); supervision (supporting); writing—review and editing (supporting). **Dmitry Baranov:** conceptualization (lead); data curation (lead); formal analysis (lead); funding acquisition (lead); investigation (lead); methodology (equal); project administration (lead); resources (lead); supervision (lead); visualization (lead); writing—original draft (lead); writing—review and editing (lead).

Data Availability Statement

The data that support the findings of this study are openly available in Zenodo at <https://zenodo.org/records/14911318>.

Keywords

crystal habit, electron microscopy, nanocrystal superlattices, optical microscopy, perovskite quantum dots, self-assembly

Received: March 3, 2025

Revised: April 10, 2025

Published online:

- [1] Z. Liu, X. Qin, Q. Chen, T. Jiang, Q. Chen, X. Liu, *Adv. Mater.* **2023**, 35, e2209279.
- [2] S. Toso, D. Baranov, U. Filippi, C. Giannini, L. Manna, *Acc. Chem. Res.* **2023**, 56, 66.
- [3] A. Dey, J. Ye, A. De, E. Debroye, S. K. Ha, E. Bladt, A. S. Kshirsagar, Z. Wang, J. Yin, Y. Wang, L. N. Quan, *ACS Nano* **2021**, 15, 10775.
- [4] S. Toso, D. Baranov, D. Altamura, F. Scattarella, J. Dahl, X. Z. Wang, S. Marras, A. P. Alivisatos, A. Singer, C. Giannini, L. Manna, *ACS Nano* **2021**, 15, 6243.
- [5] U. Filippi, S. Toso, M. L. Zaffalon, A. Pianetti, Z. Li, S. Marras, L. Goldoni, F. Meinardi, S. Brovelli, D. Baranov, L. Manna, *Adv. Mater.* **2025**, 37, e2410949.
- [6] D. N. Dirin, M. Kovalenko, *Chimia* **2024**, 78, 862.
- [7] F. Mattiotti, M. Kuno, F. Borgonovi, B. Jankó, G. L. Celardo, *Nano Lett.* **2020**, 20, 7382.
- [8] S. Ghonge, D. Engel, F. Mattiotti, G. L. Celardo, M. Kuno, B. Jankó, *Phys. Rev. Res.* **2023**, 5, 023068.
- [9] T. P. T. Nguyen, L. Z. Tan, D. Baranov, *J. Chem. Phys.* **2023**, 159, 204703.
- [10] Y. Dong, T. Qiao, D. Kim, D. Parobek, D. Rossi, D. H. Son, *Nano Lett.* **2018**, 18, 3716.
- [11] Q. A. Akkerman, T. P. T. Nguyen, S. C. Boehme, F. Montanarella, D. N. Dirin, P. Wechsler, F. Beiglbock, G. Rainò, R. Erni, C. Katan, *Science* **2022**, 377, 1406.
- [12] L. Protesescu, S. Yakunin, M. I. Bodnarchuk, F. Krieg, R. Caputo, C. H. Hendon, R. X. Yang, A. Walsh, M. V. Kovalenko, *Nano Lett.* **2015**, 15, 3692.
- [13] J. Butkus, P. Vashishtha, K. Chen, J. K. Gallaher, S. K. K. Prasad, D. Z. Metin, G. Laferensky, N. Gaston, J. E. Halpert, J. M. Hodgkiss, *Chem. Mater.* **2017**, 29, 3644.
- [14] M. A. Becker, R. Vaxenburg, G. Nedelcu, P. C. Serce, A. Shabaev, M. J. Mehl, J. G. Michopoulos, S. G. Lambrakos, N. Bernstein, J. L. Lyons, T. Stöferle, *Nature* **2018**, 553, 189.
- [15] J. Ramade, L. M. Andriambarijaona, V. Steinmetz, N. Goubet, L. Legrand, T. Barisien, F. Bernardot, C. Testelin, E. Lhiller, A. Bramati, M. Chamarro, *Nanoscale* **2018**, 10, 6393.
- [16] S. Levy, O. Be'er, S. Shaek, A. Gorchach, E. Scharf, Y. Ossia, R. Liran, K. Cohen, R. Strassberg, I. Kaminer, U. Banin, Y. Bekenstein, *ACS Nano* **2025**, 19, 963.
- [17] L. Luo, X. Tang, J. Park, C. W. Wang, M. Park, M. Khurana, A. Singh, J. Cheon, A. Belyanin, A. V. Sokolov, D. H. Son, *Nano Lett.* **2025**, 25, 6176.
- [18] S. Levy, O. Be'er, N. Veber, C. Monachon, Y. Bekenstein, *Nano Lett.* **2023**, 23, 7129.
- [19] S. C. Boehme, M. I. Bodnarchuk, M. Burian, F. Bertolotti, I. Cherniukh, C. Bernasconi, C. Zhu, R. Erni, H. Amentisch, D. Naumenko, H. Andrusiv, *ACS Nano* **2023**, 17, 2089.
- [20] C. L. Bassani, G. van Anders, U. Banin, D. Baranov, Q. Chen, M. Dijkstra, M. S. Dimitriyev, E. Efrati, J. Faraudo, O. Gang, N. Gaston, R. Golestanian, G. I. Guerrero-Garcia, M. Gruenwald, A. Haji-Akbari, M. Ibáñez, M. Karg, T. Kraus, B. Lee, R. C. Van Lehn, R. J. Macfarlane, B. M. Moggetti, A. Nikoubashman, S. Osat, O. V. Prezhdo, G. M. Rotskoff, L. Saiz, A.-C. Shi, S. Skrabalak, I. I. Smalyukh et al., *ACS Nano* **2024**, 18, 14791.
- [21] S. M. Rupich, E. V. Shevchenko, M. I. Bodnarchuk, B. Lee, D. V. Talapin, *J. Am. Chem. Soc.* **2010**, 132, 289.
- [22] X. Huang, E. Suit, J. Zhu, B. Ge, F. Gerdes, C. Klinke, Z. Wang, *J. Am. Chem. Soc.* **2023**, 145, 4500.
- [23] S. I. Stoeva, B. L. V. Prasad, S. Uma, P. K. Stoimenov, V. Zaikovski, C. M. Sorensen, K. J. Klabunde, *J. Phys. Chem. B* **2003**, 107, 7441.
- [24] A. M. Kalsin, M. Fialkowski, M. Paszewski, S. K. Smoukov, K. J. M. Bishop, B. A. Grzybowski, *Science* **2006**, 312, 420.
- [25] M. G. Constantinides, H. M. Jaeger, X. Li, J. Wang, X.-M. Lin, Z. Kristallogr. Cryst. Mater. **2007**, 222, 595.
- [26] Y. Nagaoka, K. Hills-Kimball, R. Tan, R. Li, Z. Wang, O. Chen, *Adv. Mater.* **2017**, 29, 1606666.
- [27] M. V. Kovalenko, M. I. Bodnarchuk, *Chimia* **2017**, 71, 461.
- [28] G. Rainò, M. A. Becker, M. I. Bodnarchuk, R. F. Mahrt, M. V. Kovalenko, T. Stöferle, *Nature* **2018**, 563, 671.
- [29] S. Toso, D. Baranov, C. Giannini, S. Marras, L. Manna, *ACS Mater. Lett.* **2019**, 1, 272.
- [30] Y. Tong, E.-P. Yao, A. Manzi, E. Bladt, K. Wang, M. Döblinger, S. Bals, P. Müller-Buschbaum, A. S. Urban, L. Polavarapu, J. Feldmann, *Adv. Mater.* **2018**, 30, 1801117.
- [31] H. Huang, M. W. Feil, S. Fuchs, T. Debnath, A. F. Richter, Y. Tong, L. Wu, Y. Wang, M. Döblinger, B. Nickel, *Chem. Mater.* **2020**, 32, 8877.
- [32] D. Baranov, S. Toso, M. Imran, L. Manna, M. Imran, L. Manna, *J. Phys. Chem. Lett.* **2019**, 10, 655.
- [33] D. Vila-Liarte, M. W. Feil, A. Manzi, J. L. Garcia-Pomar, H. Huang, M. Döblinger, L. M. Liz-Marzán, J. Feldmann, L. Polavarapu, A. Mihai, *Angew. Chem. Int. Ed.* **2020**, 59, 17750.
- [34] X. Li, Z. Xue, X. Chen, X. Qiao, G. Mo, W. Bu, B. Guan, T. Wang, *Sci. Adv.* **2022**, 8, eadd1559.
- [35] E. Kobiyama, D. Urbonas, B. Aymoz, M. I. Bodnarchuk, G. Rainò, A. Olziersky, D. Caimi, M. Sousa, R. F. Mahrt, M. V. Kovalenko, T. Stöferle, *ACS Nano* **2025**, 19, 6748.
- [36] Y. Tang, L. Gomez, A. Lesage, E. Marino, T. E. Kodger, J.-M. Meijer, P. Kolpakov, J. Meng, K. Zheng, T. Gregorkiewicz, P. Schall, *Nano Lett.* **2020**.
- [37] J. Nette, F. Montanarella, C. Zhu, T. Sekh, S. C. Boehme, M. Bodnarchuk, G. Raino, P. Howes, M. V. Kovalenko, A. deMello, *Chem. Commun.* **2023**, 59, 3554.
- [38] P. Tonkaev, E. Grechaninova, I. Iorsh, F. Montanarella, Y. Kivshar, M. V. Kovalenko, S. Makarov, *Nano Lett.* **2024**, 24, 2758.
- [39] D. D. Blach, V. A. Lumsargis, D. E. Clark, C. Chuang, K. Wang, L. Dou, R. D. Schaller, J. Cao, C. W. Li, L. Huang, *Nano Lett.* **2022**, 22, 7811.
- [40] Q. Wang, J. Tan, Q. Jie, H. Dong, Y. Hu, C. Zhou, S. Zhang, W. Xie, *Adv. Photonics* **2023**, 5, 055001.
- [41] H. Pashaei Adl, S. Gorji, G. Muñoz-Matutano, A. F. Gualdrón-Reyes, I. Suárez, V. S. Chirvony, I. Mora-Seró, J. P. Martínez-Pastor, *Adv. Opt. Mater.* **2023**, 11, 2202497.
- [42] Z. Liu, X. Chen, R. Yao, L. Li, H. Luo, G. Li, X. Liu, *Mater. Horiz.* **2025**, 12, 2577.
- [43] M. C. Brennan, J. E. Herr, T. S. Nguyen-Beck, J. Zinna, S. Draguta, S. Rouvimov, J. Parkhill, M. Kuno, *J. Am. Chem. Soc.* **2017**, 139, 12201.
- [44] M. Kuno, I. Gushchina, S. Toso, V. Trepalin, *J. Phys. Chem. C* **2022**, 126, 11867.
- [45] T. P. T. Nguyen, S. A. Blundell, C. Guet, *Phys. Rev. B* **2020**, 101, 195414.
- [46] F. Krieg, P. C. Serce, M. Burian, H. Andrusiv, M. I. Bodnarchuk, T. Stöferle, R. F. Mahrt, D. Naumenko, H. Amenitsch, G. Rainò, M. V. Kovalenko, *ACS Central Sci.* **2020**, 7, 135.
- [47] M. L. Timm, E. Dehdashti, A. Jarrahi Darban, H. Masoud, A. Jarrahi Darban, H. Masoud, *Sci. Rep.* **2019**, 9, 19803.
- [48] S. A. McBride, S. Dash, S. Khan, K. K. Varanasi, *Langmuir* **2019**, 35, 10484.

- [49] A. Accardo, F. Di Stasio, M. Burghammer, C. Riekel, R. Krahne, *Part. Part. Syst. Charact.* **2015**, 32, 524.
- [50] J. Desarnaud, H. Derluyn, J. Carmeliet, D. Bonn, N. Shahidzadeh, *J. Phys. Chem. Lett.* **2018**, 9, 2961.
- [51] D. Pettit, P. Fontana, *npj Microgravity* **2019**, 5, 25.
- [52] C. A. Schneider, W. S. Rasband, K. W. Eliceiri, *Nat. Methods* **2012**, 9, 671.
- [53] S. D. Park, D. Baranov, J. Ryu, B. Cho, A. Halder, S. Seifert, S. Vajda, D. M. Vajda, *Nano Lett.* **2017**, 17, 762.
- [54] D. Segets, J. M. Lucas, R. N. Klupp Taylor, M. Scheele, H. Zheng, A. P. Alivisatos, W. Peukert, *ACS Nano* **2012**, 6, 9021.
- [55] M. Gomes Ferreira, D. Baranov, *Zenodo* **2025**.
- [56] W. D. Pyrz, D. J. Buttrey, *Langmuir* **2008**, 24, 11350.
- [57] J. Kim, S. Kang, F. Cheng, Y. Wang, X. Ye, J. Park, *MRS Bull.* **2024**, 49, 365.
- [58] J. Chen, C. Yan, B. Zhu, C. Huang, F. Cheng, H. Duan, X. Ye, *Nano Res.* **2025**.
- [59] B. H. Kim, J. Heo, S. Kim, C. F. Reboul, H. Chun, D. Kang, H. Bae, H. Hyun, J. Lim, H. Lee, B. Han, *Science* **2020**, 368, 60.
- [60] D. Arenas Esteban, D. Wang, A. Kadu, N. Olluy, A. Sánchez-Iglesias, A. Gomez-Perez, J. González-Casablanca, S. Nicolopoulos, L. M. Liz-Marzán, S. Bals, *Nat. Commun.* **2024**, 15, 6399.
- [61] E. Josten, M. Angst, A. Glavic, P. Zakalek, U. Rücker, O. H. Seeck, A. Kovács, E. Wetterskog, E. Kentzinger, R. E. Dunin-Borkowski, L. Bergström, T. Brückel, *Nanoscale Horiz.* **2020**, 5, 1065.
- [62] F. Bertolotti, A. Vivani, F. Ferri, P. Anzini, A. Cervellino, M. I. Bodnarchuk, G. Nedelcu, C. Bernasconi, M. V. Kovalenko, N. Masciocchi, A. Guagliardi, *Chem. Mater.* **2022**, 34, 594.
- [63] D. Wang, M. Hermes, R. Kotni, Y. Wu, N. Tasios, Y. Liu, B. D. Nijs, E. B. van der Wee, C. B. Murray, M. Dijkstra, A. van Blaaderen, *Nat. Commun.* **2018**, 9, 2228.
- [64] J.-M. Meijer, *Colloidal Crystals of Spheres and Cubes in Real and Reciprocal Space*, Springer, New York **2015**.
- [65] J.-M. Meijer, V. Meester, F. Hagemans, H. N. W. Lekkerkerker, A. P. Philipse, A. V. Petukhov, *Langmuir* **2019**, 35, 4946.
- [66] R. Ni, A. P. Gantapara, J. De Graaf, R. Van Roij, M. Dijkstra, *Soft Matter* **2012**, 8, 8826.
- [67] A. P. Gantapara, J. De Graaf, R. Van Roij, M. Dijkstra, *Phys. Rev. Lett.* **2013**, 111, 015501.
- [68] A. P. Gantapara, J. de Graaf, R. van Roij, M. Dijkstra, *J. Chem. Phys.* **2015**, 142, 054904.
- [69] A. K. Sharma, F. A. Escobedo, *J. Chem. Phys.* **2024**, 161, 034509.
- [70] X. Xia, Y. Wang, A. Ruditskiy, Y. Xia, *Adv. Mater.* **2013**, 25, 6313.
- [71] Y. Yin, R. M. Rioux, C. K. Erdonmez, S. Hughes, G. A. Somorjai, A. P. Alivisatos, *Science* **2004**, 304, 711.
- [72] I. Fedin, D. V. Talapin, *J. Am. Chem. Soc.* **2016**, 138, 9771.
- [73] S. Kull, L. Heymann, A. B. Hungria, C. Klinke, *Chem. Mater.* **2019**, 31, 5646.
- [74] B. B. V. Salzmann, J. F. Vliem, D. N. Maaskant, L. C. Post, C. Li, S. Bals, D. Vanmaekelbergh, *Chem. Mater.* **2021**, 33, 6853.
- [75] J. Nai, B. Y. Guan, L. Yu, X. W. Lou, L. Yu, X. W. Lou, *Sci. Adv.* **2017**, 3, e1700732.
- [76] Z. Yang, J. Zhang, L. Zhang, B. Fu, P. Tao, C. Song, W. Shang, T. Deng, *Adv. Funct. Mater.* **2020**, 30, 1908108.
- [77] J. Maes, L. Balcaen, E. Drijvers, Q. Zhao, J. De Roo, A. Vantomme, F. Vanhaecke, P. Geiregat, Z. Hens, *J. Phys. Chem. Lett.* **2018**, 9, 3093.
- [78] S. Kalbfleisch, H. Neubauer, S. P. Krüger, M. Bartels, M. Osterhoff, D. D. Mai, K. Giewekemeyer, H. Neubauer, S. P. Krüger, B. Hartmann, M. Bartels, M. Sprung, O. Leupold, F. Siewert, T. Salditt, in *AIP Conf. Proc.*, American Institute of Physics, College Park **2011**, Vol. 1365, pp. 96–99.
- [79] D. Lapkin, C. Kirsch, J. Hiller, D. Andrienko, D. Assalauova, K. Braun, J. Carnis, Y. Y. Kim, M. Mandal, A. Maier, A. J. Meixner, *Nat. Commun.* **2022**, 13, 892.
- [80] I. Zaluzhnyy, R. Kurta, M. Scheele, F. Schreiber, B. Ostrovskii, I. Vartanyants, *Materials* **2019**, 12, 3464.